第51卷第8期 中国科学技术大学学报 Vol. 51, No. 8
2021年8月 JOURNAL OF UNIVERSITY OF SCIENCE AND TECHNOLOGY OF CHINA Aug. 2021
Received: 2021-04-28; Revised: 2021-05-19 doi:10.52396/JUST-2021-0121

Influence of aliovalent doping on the structure and property of Li_2MnCl_4 chloride solid electrolyte

DUAN Chaomin, MA Cheng*
Department of Materials Science & Engineering, University of Science and Technology of China, Hefei 230026, China
* Corresponding author. E-mail: mach16@ustc.edu.cn

Abstract: A series of $Li_{2-x}Mn_{1-x}Ga_xCl_4$ (x=0, 0.1, 0.3, and 0.5) materials were synthesized with the mechanochemical approach. As confirmed by X-ray powder diffraction and Rietveld refinements, Ga^{3+} can be successfully incorporated into the octahedral sites that are partially occupied by Mn^{2+}. The as-milled materials with relatively low crystallinity generally exhibit higher ionic conductivity than the well crystallized ones produced by annealing at 250 ℃. Among all the materials studied, the as-milled $Li_{1.9}Mn_{0.9}Ga_{0.1}Cl_4$ shows the highest ionic conductivity (8.3×10^{-5} S·cm^{-1}), which is two orders of magnitude higher than that of the as-milled Li_2MnCl_4 (7.12×10^{-7} S·cm^{-1}). While the unit cell volume does not vary significantly with the composition, the appropriate Li vacancy content should play an important role in the optimized ionic conductivity of $Li_{1.9}Mn_{0.9}Ga_{0.1}Cl_4$.

Keywords: aliovalent doping; chloride solid electrolyte; ionic conductivity
CLC number: TQ131.1 **Document code**: A

1 Introduction

Recently, chloride solid-state electrolytes (SSEs) have been proven a promising candidate for application in all-solid-state Li batteries (ASSBs), because they show a rare combination of high ionic conductivity, excellent deformability, and good compatibility with the 4 V-class cathodes[1-6]. Nevertheless, recent studies are almost exclusively focused on the materials based on Li_3YCl_6 and Li_3InCl_6[7], while another large family of chloride systems, Li_2MCl_4 (M=Mn, Fe, Co, etc.), was barely investigated.

The existing studies on Li_2MCl_4 are rare and most of them were reported about 20 years ago[7-12]. The vast majority of Li_2MCl_4 shows the inverse spinel structure (space group $Fd\bar{3}m$). In this structure, a part of Li ions occupy the tetrahedral sites, while the remaining Li^+ and all of the M^{2+} reside on the octahedral sites[13,14]. Among all the Li_2MCl_4 materials, Li_2MnCl_4 exhibits a relatively high ionic conductivity of 4×10^{-6} S·cm^{-1}[13]. Besides, some studies show that the ionic conductivity of Li_2MnCl_4 can be improved by doping[12] or compositing with CeO_2[15], which means that there is room for further improvement of its ionic conductivity. Considering that many Li_2MCl_4 solid electrolytes are isostructural with Li_2MnCl_4, they should exhibit a similar Li-ion migration behavior; the investigation on Li_2MnCl_4 would thus also shed light on the ionic transport mechanism of other isostructural Li_2MCl_4 systems. Among the various characteristics of Li_2MnCl_4, the variation of its conductivity with aliovalent doping is particularly interesting, because this is a very commonly adopted approach for tailoring the ionic transport behavior of solid electrolytes, and also very important information to comprehend the ionic transport mechanism. However, this issue has not been systematically studied in the existing reports[9,12,14,16].

In this work, we explore the influence of aliovalent doping on the ionic transport behavior of Li_2MnCl_4. With divalent Mn^{2+} partially substituted by trivalent Ga^{3+}, aliovalently-doped $Li_{2-x}Mn_{1-x}Ga_xCl_4$ (x = 0.1, 0.3, 0.5) were synthesized and orders of magnitude conductivity improvement with respect to unmodified Li_2MnCl_4 was observed. The mechanism behind such optimized conductivity is also discussed based on the crystal structures acquired from Rietveld refinement.

2 Experiments

2.1 Synthesis of $Li_{2-x}Mn_{1-x}Ga_xCl_4$ (x=0, 0.1, 0.3, 0.5)

The samples were prepared by high energy ball-milling and annealing methods. The starting materials are LiCl

Citation: Duan Chaomin, Ma Cheng. Influence of aliovalent doping on the structure and property of Li_2MnCl_4 chloride solid electrolyte. J. Univ. Sci. Tech. China, 2021, 51(8): 628-636.

(Alfa Aesar, 99.99%), $MnCl_2$ (Aladdin, 99.9%) and $GaCl_3$ (Aladdin, 99.99%). For the ball-milling process, stoichiometric amount of LiCl, $MnCl_2$ and $GaCl_3$ were hand-mixed in the mortar by pestle for homogenization. Subsequently, the as-mixed stoichiometric mixture was loaded into tungsten carbide (WC) pots with 5 mm-diameter WC balls. The ball to the powder weight ratio was 25∶1 and the rotating speed was set to 500 r/min. All the aforementioned procedures were conducted in the glove box filled with Ar to avoid possible water-absorption of raw materials. After milling over 20 h, corresponding as-milled $Li_{2-x}Mn_{1-x}Ga_xCl_4$ (x=0, 0.1, 0.3, 0.5) powder samples were obtained. To synthesize the well-crystallized samples, the as-milled powder was conducted with annealing. Prior to annealing, the as-milled powder was cold-pressed into a pellet and then loaded into the borosilicate glass tube in the glove box. Subsequently, the glass tube loaded with the as-pressed pellet sample was evacuated and sealed by vacuum sealing apparatus. Finally, the sealed glass tube with the as-pressed pellet was transferred to furnace for annealing. Specifically, the $Li_{2-x}Mn_{1-x}Ga_xCl_4$ (x=0, 0.1, 0.3, 0.5) pellets were heated at 250 °C for 5 h.

2.2 Structure characterization

The structure information was obtained from X-ray powder diffraction (XRD) by means of X- ray powder diffractometer (Rigaku, Ultima IV) using Cu Kα1 radiation. Prior to XRD measurements, the powder was sealed in the sample holder by Kapton film in the glove box filled with Ar atmosphere considering its hygroscopic nature. The scanning speed was 5 degree per minute and the scanning range was from 20° to 80°. Rietveld refinements were conducted using the GSAS-II software[17]. The structure was refined with the U_{iso} limited to positive values and stoichiometry confined to the nominal ones; under these restraint conditions, the occupancy of each atomic site is allowed to vary freely during refinement.

2.3 Electrochemical characterization

For samples without heat-treatment, the powder sample was first cold-pressed under 400 MPa into the pellet for electrochemical measurements. For the annealed sample, the sample was hand-ground into powder and then cold-pressed under 400 MPa into the pellet again. Prior to electrochemical impedance spectroscopy (EIS) measurements, the as-pressed pellet was coated with Au on the two sides as blocking electrode by ion sputter apparatus. All the steps mentioned above were conducted in the glove box filled with Ar. Finally, the pellet coated with Au was sealed in a home-made apparatus tailored to EIS measurements. The frequency range was from 1 Hz to 7 MHz and the amplitude voltage was 50 mV. All the EIS measurements were performed using the electrochemical impedance analyzer (Biologic, MTZ-35) at 25 °C. The ionic conductivity value was calculated by the standard formula, $\sigma = \frac{t}{RS}$, where t is the thickness of the pellet, $S$is the area of the pellet and R denotes the resistance value determined by the EIS measurements. The R value was determined by the intercept of the curve with real part of impedance extrapolated from the point where the absolute value of imaginary part is the lowest. The impedance spectra were fitted using Zview software.

3 Results and discussions

XRD patterns of the as-milled $Li_{2-x}Mn_{1-x}Ga_xCl_4$ powder samples are shown in Figure 1(a). For each XRD pattern of as-milled $Li_{2-x}Mn_{1-x}Ga_xCl_4$, it can be well indexed into PDF#51-0304 corresponding to diffraction pattern of Li_2MnCl_4. Based on the analysis of XRD measurements results, two points can be concluded. One is that Ga^{3+} have been successfully incorporated into crystal lattice of Li_2MnCl_4 since there are no appreciable impurity peaks in the XRD patterns of the as-milled samples and the diffraction peaks of the doped samples are in the same position as Li_2MnCl_4. The other one is the low crystallinity inferred from the broad diffraction peaks, making it hard to obtain detailed information on the crystal structure. Thus, the annealed samples with high crystallinity were conducted with XRD measurements and the results are shown in Figure 1(b). All the XRD patterns of annealed $Li_{2-x}Mn_{1-x}Ga_xCl_4$ (x= 0, 0.1, 0.3) can be in line with PDF#51-0304 whereas some unindexable tiny impurity peaks were observed for the annealed $Li_{1.5}Mn_{0.5}Ga_{0.5}Cl_4$. Therefore, we can conclude that the mutual solubility of $Li_{2-x}Mn_{1-x}Ga_xCl_4$ is somewhat larger than 0.3 but less than 0.5. As for the reason why no such impurity peaks were observed in the XRD patterns of the as-milled $Li_{1.5}Mn_{0.5}Ga_{0.5}Cl_4$, a plausible explanation is that the diffraction intensity of impurities is so weak for the as-milled sample that the impurity peaks are covered by noises from the X-ray powder diffractometer and thus cannot be distinguished.

From the aforementioned discussions, we preliminarily confirm that the aliovalently doped $Li_{2-x}Mn_{1-x}Ga_xCl_4$ samples have been successfully synthesized as expected. To determine precise crystal structure parameters, Rietveld refinements were performed on the XRD patterns of both as-milled and annealed $Li_{2-x}Mn_{1-x}Ga_xCl_4$ samples and the corresponding results are given in Figure 2 and Figure 3. All of the R_{wp} values of refinements for both as-milled and annealed $Li_{2-x}Mn_{1-x}Ga_xCl_4$ are acceptably low,

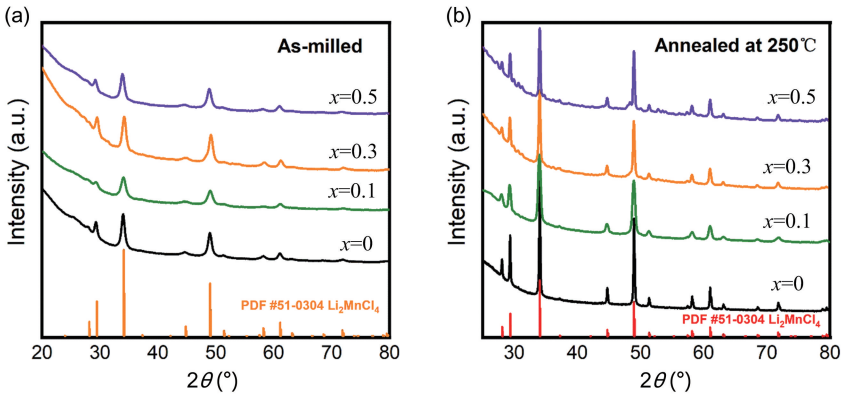

Figure 1. XRD patterns of ball-milled (a) and annealed (b) $Li_{2-x}Mn_{1-x}Ga_xCl_4$ powder samples. In both Figure1(a) and Figure 1(b), the black curve, green curve, yellow curve and violet curve correspond to $x=0$, $x=0.1$, $x=0.3$ and $x=0.5$ for $Li_{2-x}Mn_{1-x}Ga_xCl_4$, respectively.

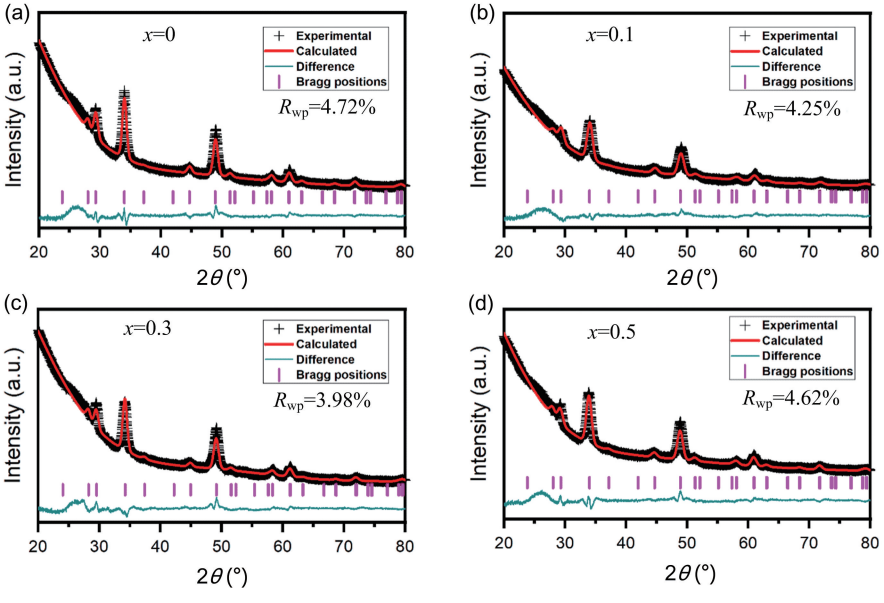

Figure 2. Rietveld refinements on XRD patterns of as-milled $Li_{2-x}Mn_{1-x}Ga_xCl_4$ powder samples. (a), (b), (c) and (d) correspond to $x=0$, $x=0.1$, $x=0.3$ and $x=0.5$ for $Li_{2-x}Mn_{1-x}Ga_xCl_4$, respectively. Dark cross symbols correspond to experimental data. The red curve corresponds to the calculated pattern. Pink lines correspond to Bragg positions. The light green curve corresponds to the difference between calculated patterns and experimental data.

indicating high credibility of the Rietveld refinements results. In this case, we can obtain reasonably reliable information on the crystal structure of $Li_{2-x}Mn_{1-x}Ga_xCl_4$ as shown in Tables 1−8. Note that the fitting uncertainty is given in brackets. For Li_2MnCl_4 without substitution, there are two different sites of lithium. A part of Li^+ fully occupy the tetrahedral ($8a$) sites surrounded by four chloride ions while the rest are located at octahedral ($16d$) sites surrounded by six chloride ions. All the Mn^{2+} are distributed over the same octahedral ($16d$) sites as the part of Li^+. All the Cl^- are located at $32e$ sites. For doped $Li_{2-x}Mn_{1-x}Ga_xCl_4$, Ga^{3+} are incorporated into octahedral ($16d$) sites. In the meantime, the tetrahedral ($8a$) sites are no longer fully occupied by Li^+ in order to keep the charge balance, leading to increased number of vacancies. Correspondingly, the octahedral sites are simultaneously accommodating Li^+, Mn^{2+} and Ga^{3+}. Furthermore, with Ga^{3+} incorporated into the crystal structure of Li_2MnCl_4, the number of vacancies increases while Li^+ concentration decreases at the same time. In addition to the change of cation site occupation, the unit cell parameter has also varied with the composition of $Li_{2-x}Mn_{1-x}Ga_xCl_4$. However, the difference of lattice parameters between the as-milled and annealed samples is insignificant for $Li_{2-x}Mn_{1-x}Ga_xCl_4$ ($x=0$, 0.1, 0.3, 0.5).

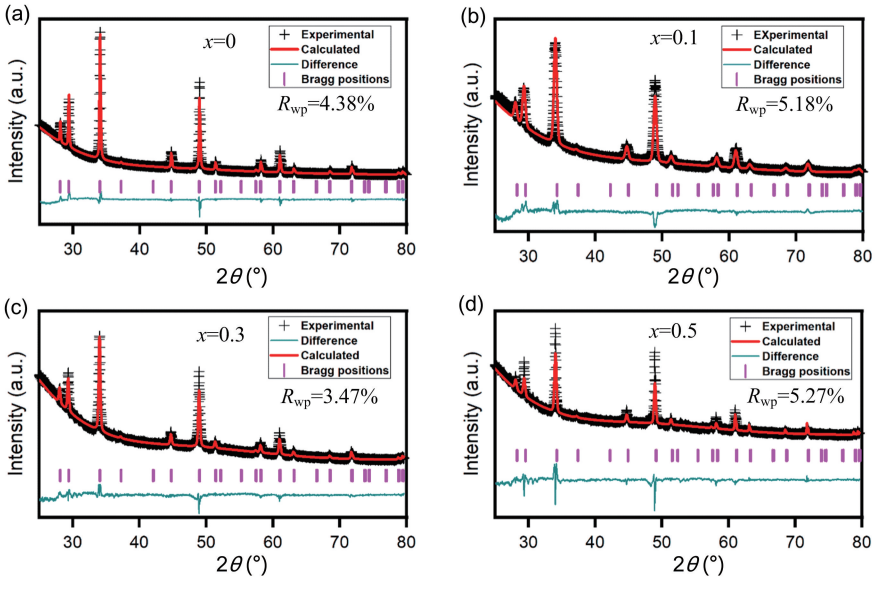

Figure 3. Rietveld refinements on XRD patterns of annealed $Li_{2-x}Mn_{1-x}Ga_xCl_4$ powder samples. (a), (b), (c) and (d) correspond to $x=0$, $x=0.1$, $x=0.3$ and $x=0.5$ for $Li_{2-x}Mn_{1-x}Ga_xCl_4$, respectively. Dark cross symbols correspond to the experimental data. Red curve corresponds to the calculated pattern. Pink lines correspond to Bragg positions. The light green curve corresponds to the difference between calculated patterns and experimental data.

Table 1. Rietveld analysis results for the XRD patterns of as-milled Li_2MnCl_4.

Space group $Fd\bar{3}m$
$a=b=c=10.50208(8)$ Å, $\alpha=\beta=\gamma=90°$
Fit residuals: $R_{wp}=4.72\%$, $R_p=3.66\%$

Atom	Site	x	y	z	Occupancy	U_{iso}
Li1	8a	1/8	1/8	1/8	1	0.0173(9)
Li2	16d	1/2	1/2	1/2	0.5	0.0221(11)
Mn2	16d	1/2	1/2	1/2	0.5	0.0373(11)
Cl1	32e	0.25509(29)	0.25509(29)	0.25509(29)	1	0.0147(3)

Table 2. Rietveld analysis results for the XRD patterns of annealed Li_2MnCl_4.

Space group $Fd\bar{3}m$
$a=b=c=10.50243(16)$ Å, $\alpha=\beta=\gamma=90°$
Fit residuals: $R_{wp}=4.38\%$, $R_p=3.27\%$

Atom	Site	x	y	z	Occupancy	U_{iso}
Li1	8a	1/8	1/8	1/8	1	0.0170(9)
Li2	16d	1/2	1/2	1/2	0.5	0.0113(4)
Mn2	16d	1/2	1/2	1/2	0.5	0.0308(12)
Cl1	32e	0.25686(15)	0.25686(15)	0.25686(15)	1	0.0311(9)

Table 3. Rietveld analysis results for the XRD patterns of as-milled $Li_{1.9}Mn_{0.9}Ga_{0.1}Cl_4$.

Space group $Fd\bar{3}m$
$a=b=c=10.50169(13)$ Å, $\alpha=\beta=\gamma=90°$
Fit residuals: $R_{wp}=4.25\%$, $R_p=3.41\%$

Atom	Site	x	y	z	Occupancy	U_{iso}
Li1	8a	1/8	1/8	1/8	0.90(10)	0.0048(9)
Li2	16d	1/2	1/2	1/2	0.50(15)	0.0301(4)
Mn2	16d	1/2	1/2	1/2	0.45(21)	0.0115(12)
Ga2	16d	1/2	1/2	1/2	0.050(6)	0.0032(7)
Cl1	32e	0.25783(31)	0.25783(31)	0.25783(31)	1.000(19)	0.01458(21)

Table 4. Rietveld analysis results for the XRD patterns of annealed $Li_{1.9}Mn_{0.9}Ga_{0.1}Cl_4$.

Space group $Fd\bar{3}m$
$a=b=c=10.50222(4)$ Å, $\alpha=\beta=\gamma=90°$
Fit residuals: $R_{wp}=5.18\%$, $R_p=3.97\%$

Atom	Site	x	y	z	Occupancy	U_{iso}
Li1	8a	1/8	1/8	1/8	0.90(17)	0.031(4)
Li2	16d	1/2	1/2	1/2	0.50(13)	0.0199(14)
Mn2	16d	1/2	1/2	1/2	0.45(2)	0.0142(8)
Ga2	16d	1/2	1/2	1/2	0.05(3)	0.0137(11)
Cl1	32e	0.2567(2)	0.2567(2)	0.2567(2)	1.000(17)	0.0051(4)

Table 5. Rietveld analysis results for the XRD patterns of as-milled $Li_{1.7}Mn_{0.7}Ga_{0.1}Cl_4$.

Space group $Fd\bar{3}m$
$a=b=c=10.50190(9)$ Å, $\alpha=\beta=\gamma=90°$
Fit residuals: $R_{wp}=3.98\%$, $R_p=3.05\%$

Atom	Site	x	y	z	Occupancy	U_{iso}
Li1	8a	1/8	1/8	1/8	0.70(11)	0.0019(3)
Li2	16d	1/2	1/2	1/2	0.50(6)	0.0013(7)
Mn2	16d	1/2	1/2	1/2	0.35(10)	0.0038(31)
Ga2	16d	1/2	1/2	1/2	0.15(7)	0.0041(9)
Cl1	32e	0.25243(41)	0.25243(41)	0.25243(41)	1.00(5)	0.0045(15)

Table 6. Rietveld analysis results for the XRD patterns of annealed $Li_{1.7}Mn_{0.7}Ga_{0.1}Cl_4$.

Space group $Fd\bar{3}m$
$a=b=c=10.50268(30)$ Å, $\alpha=\beta=\gamma=90°$
Fit residuals: $R_{wp}=3.47\%$, $R_p=2.74\%$

Atom	Site	x	y	z	Occupancy	U_{iso}
Li1	8a	1/8	1/8	1/8	0.70(15)	0.0047(9)
Li2	16d	1/2	1/2	1/2	0.50(7)	0.0031(11)
Mn2	16d	1/2	1/2	1/2	0.3500(27)	0.013(7)
Ga2	16d	1/2	1/2	1/2	0.1500(27)	0.04(4)
Cl1	32e	0.25574(26)	0.25574(26)	0.25574(26)	1.0000(14)	0.0027(12)

Table 7. Rietveld analysis results for the XRD patterns of as-milled $Li_{1.5}Mn_{0.5}Ga_{0.5}Cl_4$.

Space group $Fd\bar{3}m$
$a=b=c=10.50202(10)$ Å, $\alpha=\beta=\gamma=90°$
Fit residuals: $R_{wp}=4.62\%$, $R_p=3.66\%$

Atom	Site	x	y	z	Occupancy	U_{iso}
Li1	8a	1/8	1/8	1/8	0.50(5)	0.013(2)
Li2	16d	1/2	1/2	1/2	0.50(7)	0.0200(18)
Mn2	16d	1/2	1/2	1/2	0.25(2)	0.0312(3)
Ga2	16d	1/2	1/2	1/2	0.25(8)	0.0178(5)
Cl1	32e	0.25473(34)	0.25473(34)	0.25473(34)	1.000(6)	0.0373(12)

Table 8. Rietveld analysis results for the XRD patterns of annealed $Li_{1.5}Mn_{0.5}Ga_{0.5}Cl_4$.

Space group $Fd\bar{3}m$
$a=b=c=10.50277$ Å, $\alpha=\beta=\gamma=90°$
Fit residuals: $R_{wp}=5.27\%$, $R_p=3.60\%$

Atom	Site	x	y	z	Occupancy	U_{iso}
Li1	8a	1/8	1/8	1/8	0.50(13)	0.0154(17)
Li2	16d	1/2	1/2	1/2	0.50(4)	0.0015(7)
Mn2	16d	1/2	1/2	1/2	0.250(12)	0.0399(12)
Ga2	16d	1/2	1/2	1/2	0.250(7)	0.0044(11)
Cl1	32e	0.25660(34)	0.25660(34)	0.25660(34)	1.000(11)	0.0071(9)

The ionic conductivities of $Li_{2-x}Mn_{1-x}Ga_xCl_4$ were measured by electrochemical impedance spectroscopy (EIS). Figure 4(a) and Figure 4(b) show the Nyquist plots of the EIS measurements. The real part and the imaginary part are normalized by the thickness and area of the sample for the test. In the Nyquist plots, there is only one semicircle at high frequency, suggesting that the grain-boundary resistance is not large enough to induce an individual semicircle. The impedance spectra were fitted with an equivalent circuit comprising a parallel constant phase element (CPE) and a resistor (R) in series with the CPE. The R component includes both the grain-bulk and grain-boundary resistance of the pellet. The comparison of ionic conductivities and compositions of $Li_{2-x}Mn_{1-x}Ga_xCl_4$ is given in Figure 4 (c) and Figure 4 (d) for as-milled and annealed samples, respectively. Note that the left axis represents $\log(\sigma)$ instead of σ. For as-milled samples, the ionic conductivities first increase significantly and then drop slightly when the concentration of Ga^{3+} increases. In the case of annealed samples, the ionic conductivity generally follows the same trend as that of the as-milled counterpart. For both as-milled and annealed samples, the ionic conductivity reaches the maximum when $x=0.1$ for $Li_{2-x}Mn_{1-x}Ga_xCl_4$. From the perspective of the unit cell volume, a large cell volume typically facilitates the ionic conduction. However, interestingly, the trend of the change of the cell volume is opposite to that of ionic conductivity as depicted by the black lines in Figure 4(c) and Figure 4(d). It seems to be counter-intuitive at the first glance. Nevertheless, notice that the right y axis ranges from 1157 $Å^3$ to 1159 $Å^3$ in Figure 4 (c) while it ranges 1158 $Å^3$ to 1159 $Å^3$ in Figure 4(d). For as-milled samples, the relative variation ratio of the cell volume is merely 3.26×10^{-4}, which is negligible compared to the dramatic variation of ionic conductivity (from 10^{-7} to 10^{-5} S · cm^{-1} order of magnitude). Besides, as illustrated in Figure 4(c) and Figure 4(d), error bars of the cell volume obtained from Rietveld refinements are all within a relatively wide range, especially for the as-milled samples, indicating the fluctuation of the cell volume of $Li_{2-x}Mn_{1-x}Ga_xCl_4$ is likely insignificant. Therefore, the trivial difference of cell volume is not the dominant factor that governs the ionic conduction properties of $Li_{2-x}Mn_{1-x}Ga_xCl_4$. As can be seen from Figure 4, the variation of ionic conductivity with the aliovalent doping is significant, especially for the as-milled samples, which range from 10^{-7} to 10^{-5} S · cm^{-1}, indicating that aliovalent doping is an effective way of tuning the ionic conductivity of

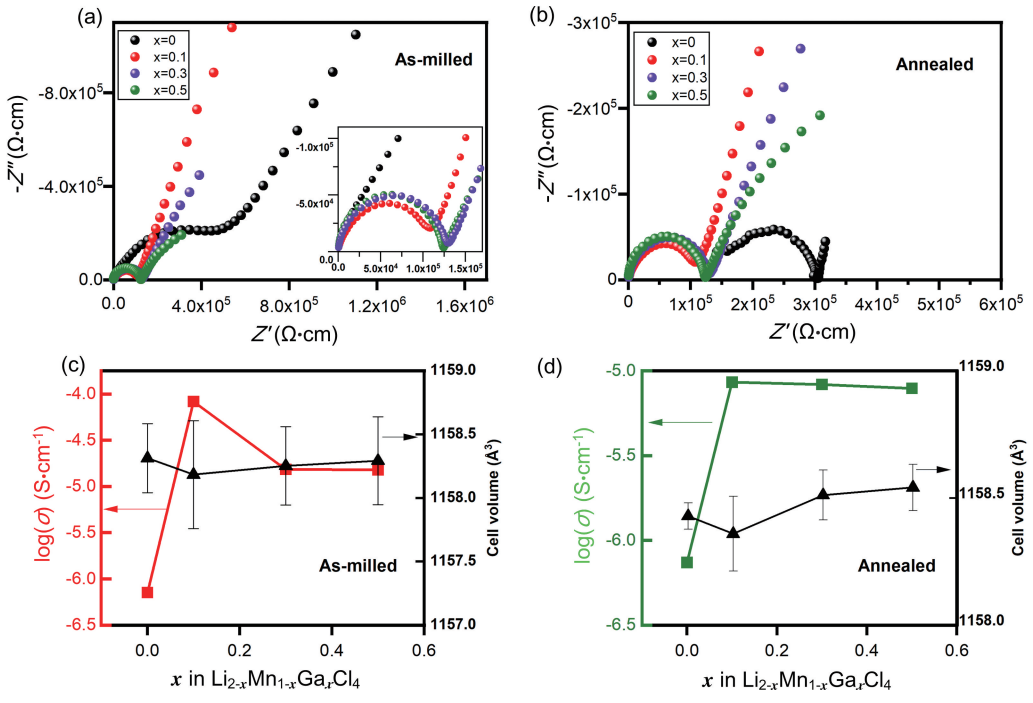

Figure 4. Electrochemical measurements of ball-milled and annealed $Li_{2-x}Mn_{1-x}Ga_xCl_4$ samples. (a) Nyquist plots of ball-milled $Li_{2-x}Mn_{1-x}Ga_xCl_4$ samples; (b) Nyquist plots of annealed $Li_{2-x}Mn_{1-x}Ga_xCl_4$ samples; (c) ionic conductivities (red line)/cell volume (black line, the vertical line is error bar) versus compositions of ball-milled $Li_{2-x}Mn_{1-x}Ga_xCl_4$; (d) ionic conductivities (green line, the vertical line is error bar) /cell volume (black line) versus compositions of annealed $Li_{2-x}Mn_{1-x}Ga_xCl_4$.

Li_2MnCl_4. It can be inferred from Figure 4 that the ionic conductivities of the doped $Li_{2-x}Mn_{1-x}Ga_xCl_4$ (x = 0.1, 0.3, 0.5) decrease after annealing while the ionic conductivity of the undoped Li_2MnCl_4 increases slightly with the improvement of crystallinity. The mechanochemical synthesized samples are considered to possess cation partially disordered structure[5]. Since the blocking effect of Ga^{3+} and Mn^{2+} on Li^+ mobility may be eased in the case of a structure with partially disordered cations resulted from mechanochemical synthesis[18], the as-milled samples as thus deliver ionic conductivities higher than the annealed counterparts. As confirmed by Rietveld refinements on XRD patterns, all the substituted $Li_{2-x}Mn_{1-x}Ga_xCl_4$ possess the same inverse spinel structure (space group of $Fd\bar{3}m$) as Li_2MnCl_4. Furthermore, as discussed in the section of XRD measurements, when x in $Li_{2-x}Mn_{1-x}Ga_xCl_4$ increases, an increase in the number of vacancies and a decrease in the concentration of Li^+ are accompanied. Typically, a high vacancy content is beneficial to high Li-ion mobility whereas a limited Li^+ concentration will impede ionic conduction. Thus, these two mechanisms impact in opposite ways on the ionic conductivities of $Li_{2-x}Mn_{1-x}Ga_xCl_4$. Therefore, a balance between these two mechanisms is expected to be observed. Indeed, the balance has been established by EIS measurements as shown in Figure 4. With x = 0.1, $Li_{2-x}Mn_{1-x}Ga_xCl_4$ exhibits the highest ionic conductivity among all the other counterparts. The analysis above may shed light on the behavior of the ionic conductivity versus the composition of $Li_{2-x}Mn_{1-x}Ga_xCl_4$. Unmodified Li_2MnCl_4 shows mediocre ionic conductivity compared to doped ones, which is presumably due to limited available vacancies for Li^+ hopping as evidenced by fully occupied tetrahedral sites. When the content of Ga^{3+} is relatively low ($0 < x \leqslant 0.1$), the concentration of vacancies for Li^+ hopping influences ionic conduction prominently. As a result, a significant improvement in ionic conductivity can be observed when Li_2MnCl_4 is doped with low content of Ga^{3+} (x = 0.1). However, with fraction of Ga^{3+} increasing further ($0.1 < x \leqslant 0.5$), the depleted Li^+ carrier concentration plays a predominant role and thus lowers the ionic conductivity. Therefore, when $0.1 < x \leqslant 0.5$, the ionic conductivity decreases with increasing x in $Li_{2-x}Mn_{1-x}Ga_xCl_4$, as illustrated in Figure 4(c, d).

4 Conclusions

In summary, aliovalent doping has been demonstrated to be an effective way of improving ionic conductivity of Li_2MnCl_4. Using the X-ray diffraction, the partial substitution of Mn^{2+} by Ga^{3+} in the lattice has been confirmed. The as-milled materials generally show higher conductivities than the annealed ones with high

crystallinity. The as-milled $Li_{1.9}Mn_{0.9}Ga_{0.1}Cl_4$ was observed to show the highest ionic conductivity (8.3×10^{-5} S · cm^{-1}) among all the $Li_{2-x}Mn_{1-x}Ga_xCl_4$ samples, two orders of magnitude higher than the 7.12×10^{-7} S · cm^{-1} conductivity for the as-milled Li_2MnCl_4. The highest conductivity achieved for $Li_{1.9}Mn_{0.9}Ga_{0.1}Cl_4$ is due to the balance between the Li^+ concentration and vacancies available for Li^+ hopping, which should receive close attention in future studies of Li_2MCl_4-based solid electrolytes.

Acknowledgments

This work was supported by the National Key R&D Program of China (2018YFA0209600, 2017YFA0208300), the National Natural Science Foundation of China (51802302), and the Fundamental Research Funds for the Central Universities (WK3430000006).

Conflict of interest

The authors declare no conflict of interest.

Author information

DUAN Chaomin received his Bachelor's degree from Hefei University of Technology in 2018 and is currently a Master student at University of Science and Technology of China (USTC). His main research interests focus on all-solid-state batteries and halide solid state electrolytes.

MA Cheng (corresponding author) received his BS degree in Materials Science and Engineering in 2006 from Tsinghua University (Beijing, China) and PhD degree in Materials Science and Engineering in 2012 from Iowa State University. After completing his work as a postdoctoral researcher at the Oak Ridge National Laboratory in 2016, he joined USTC as a professor. His research interest lies in the critical materials and interfaces in all-solid-state Li batteries.

References

[1] Asano T, Sakai A, Ouchi S, et al. Solid halide electrolytes with high lithium-ion conductivity for application in 4 V class bulk-type all-solid-state batteries. Advanced Materials, 2018, 30: 1803075.

[2] Li X N, Liang J W, Luo J, et al. Air-stable Li_3InCl_6 electrolyte with high voltage compatibility for all-solid-state batteries. Energy & Environmental Science, 2019, 12: 2665-2671.

[3] Li X N, Liang J W, Adair K R, et al. Origin of superionic $Li_3Y_{1-x}In_xCl_6$ halide solid electrolytes with high humidity tolerance. Nano Letters, 2020, 20: 4384-4392.

[4] Liang J W, Li X N, Wang S, et al. Site-occupation-tuned superionic Li_xScCl_{3+x} halide solid electrolytes for all-solid-state batteries. Journal of the American Chemical Society, 2020, 142: 7012-7022.

[5] Schlem R, Muy S, Prinz N, et al. Mechanochemical synthesis: A tool to tune cation site disorder and ionic transport properties of Li_3MCl_6 (M = Y, Er) superionic conductors. Advanced Energy Materials, 2020, 10: 1903719.

[6] Kwak H, Han D, Lyoo J, et al. New cost-effective halide solid electrolytes for all-solid-state batteries: Mechanochemically prepared Fe^{3+}-substituted Li_2ZrCl_6. Advanced Energy Materials, 2021, 11: 2003190.

[7] Kanno R, Takeda Y, Yamamoto O. Ionic-conductivity of solid lithium ion conductors with the spinel structure: Li_2MCl_4 (M = Mg, Mn, Fe, Cd). Materials Research Bulletin, 1981, 16: 999-1005.

[8] Lutz H D, Schmidt W, Haeuseler H. Chloride spinels: A new group of solid lithium electrolytes. Journal of Physics and Chemistry of Solids, 1981, 42: 287-289.

[9] Kanno R, Takeda Y, Takada K, et al. Ionic-conductivity and phase-transition of the spinel system $Li_{2-2x}M_{1+x}Cl_4$ (M= Mg, Mn, Cd). Journal of the Electrochemical Society, 1984, 131: 469-474.

[10] Kanno R, Takeda Y, Matsumoto A, et al. Synthesis, structure, ionic-conductivity, and phase-transformation of new double chloride spinel, Li_2CrCl_4. Journal of Solid State Chemistry, 1988, 75: 41-51.

[11] Lutz H D, Pfitzner A, Cockcroft J K. Structural phase-transition and nonstoichiometry of Li_2FeCl_4-neutron diffraction studies. Journal of Solid State Chemistry, 1993, 107: 245-249.

[12] Wickel C, Zhang Z, Lutz H D. Crystal-structure and electric-conductivity of spinel-type $Li_{2-2x}Mn_{1+x}Cl_4$ solid-solutions. Zeitschrift für anorganische und allgemeine Chemie, 1994, 620: 1537-1542.

[13] Cros C, Hanebali L, Latie L, et al. Structure, ionic motion and conductivity in some solid-solutions of the LiCl-MCl_2 systems (M = Mg, V, Mn). Solid State Ionics, 1983, 9-10:139-147.

[14] Lutz H D, Steiner H J, Wickel C. Fast ionic conductivity and crystal structure of spinel-type $Li_{2-x}Mn_{1-x}M_xCl_4$ (M = Ga, In). Solid State Ionics, 1997, 95: 173-181.

[15] Jacob M M E, Rajendran S, Gangadharan R, et al. Effect of dispersion of CeO_2 in the ionic conductivity of Li_2MnCl_4. Solid State Ionics, 1996, 86-88: 595-602.

[16] Soubeyroux J L, Cros C, Gang W, et al. Neutron-diffraction investigation of the cationic distribution in the structure of the spinel-type solid-solutions $Li_{2-2x}M_{1+x}Cl_4$ (M = Mg, V): Correlation with the ionic-conductivity and NMR data. Solid State Ionics, 1985, 15: 293-300.

[17] Toby B H, Von Dreele R B. GSAS-II: the genesis of a modern open-source all purpose crystallography software package. Journal of Applied Crystallography, 2013, 46: 544-549.

[18] Yabuuchi N, Hara R, Kajiyama M, et al. New O2/P2-type Li-excess layered manganese oxides as promising multi-functional electrode materials for rechargeable Li/Na batteries. Advanced Energy Materials, 2014, 4: 1301453.

异价掺杂对 Li_2MnCl_4 氯化物固态电解质结构和性能的影响

段超民,马骋*
中国科学技术大学材料科学与工程系,安徽合肥 230026
*通讯作者. E-mail:mach16@ustc.edu.cn

摘要:一系列 $Li_{2-x}Mn_{1-x}Ga_xCl_4$(x=0, 0.1, 0.3, 0.5)可以通过机械化学的方法合成. 根据 X 射线衍射以及 Rietveld 结构精修,Ga^{3+} 成功进入了被 Mn^{2+} 部分占据的八面体位点. 刚经过球磨的、具有较低结晶度的材料整体上在离子电导率方面优于结晶良好、经过 250 ℃退火的材料. 刚经过球磨的 $Li_{1.9}Mn_{0.9}Ga_{0.1}Cl_4$ 在所有样品中展现出了最高的离子电导率(8.3×10^{-5} S·cm^{-1}),比刚球磨过的 Li_2MnCl_4(7.12×10^{-7} S·cm^{-1})高两个数量级. 由于晶胞尺寸并没有随着成分发生显著变化,$Li_{1.9}Mn_{0.9}Ga_{0.1}Cl_4$ 的最优离子电导率应主要来源于合适的 Li 空位含量.

关键词:异价掺杂;氯化物固态电解质;离子电导率